

Supplementary Information for: Reordering Transitions during Annealing of Block Copolymer Cylinder Phases

Pawel W. Majewski, Kevin G. Yager*

*Center for Functional Nanomaterials, Brookhaven National Laboratory, Upton, New York
11973, USA*

email: kyager@bnl.gov

GISAXS of Oven Annealed Thin Films

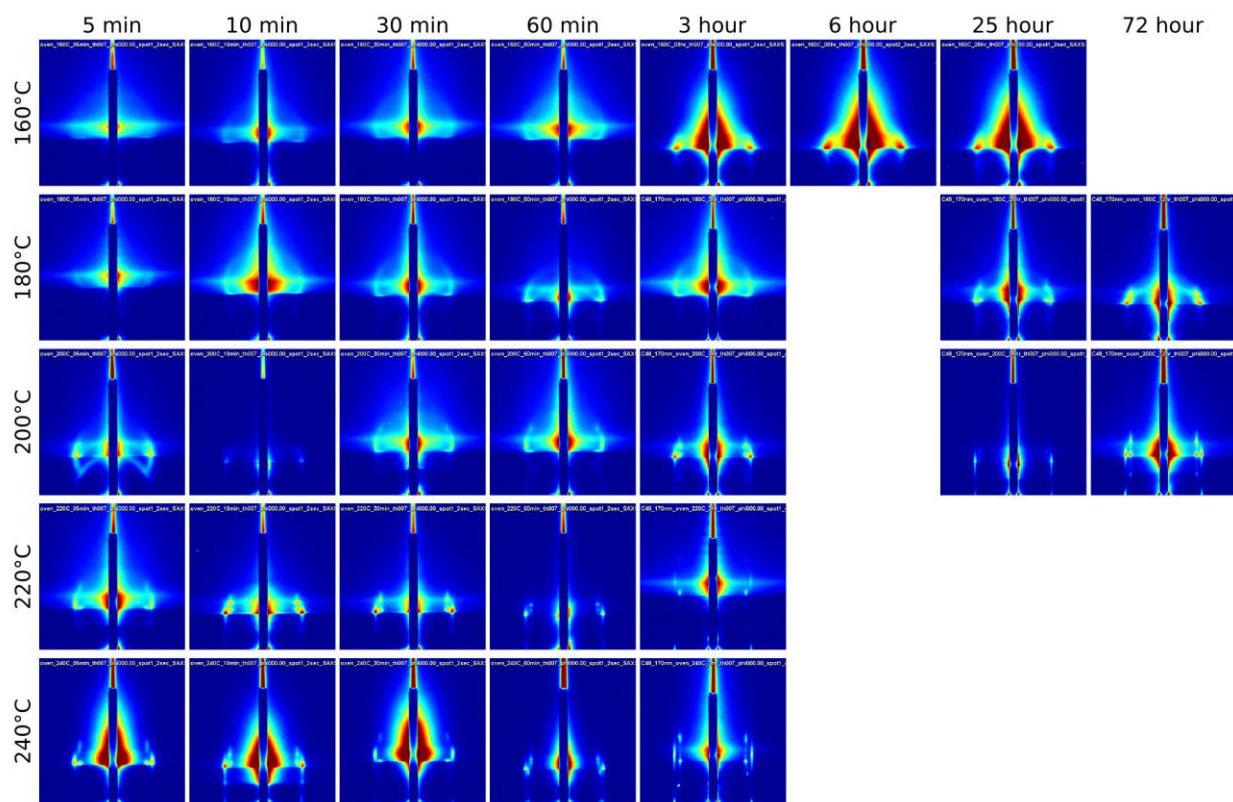


Figure S1: GISAXS of BCP thin films, measured at $\vartheta = 0.07^\circ$. These measurements are below the film-vacuum critical angle, and are thus surface-sensitive.

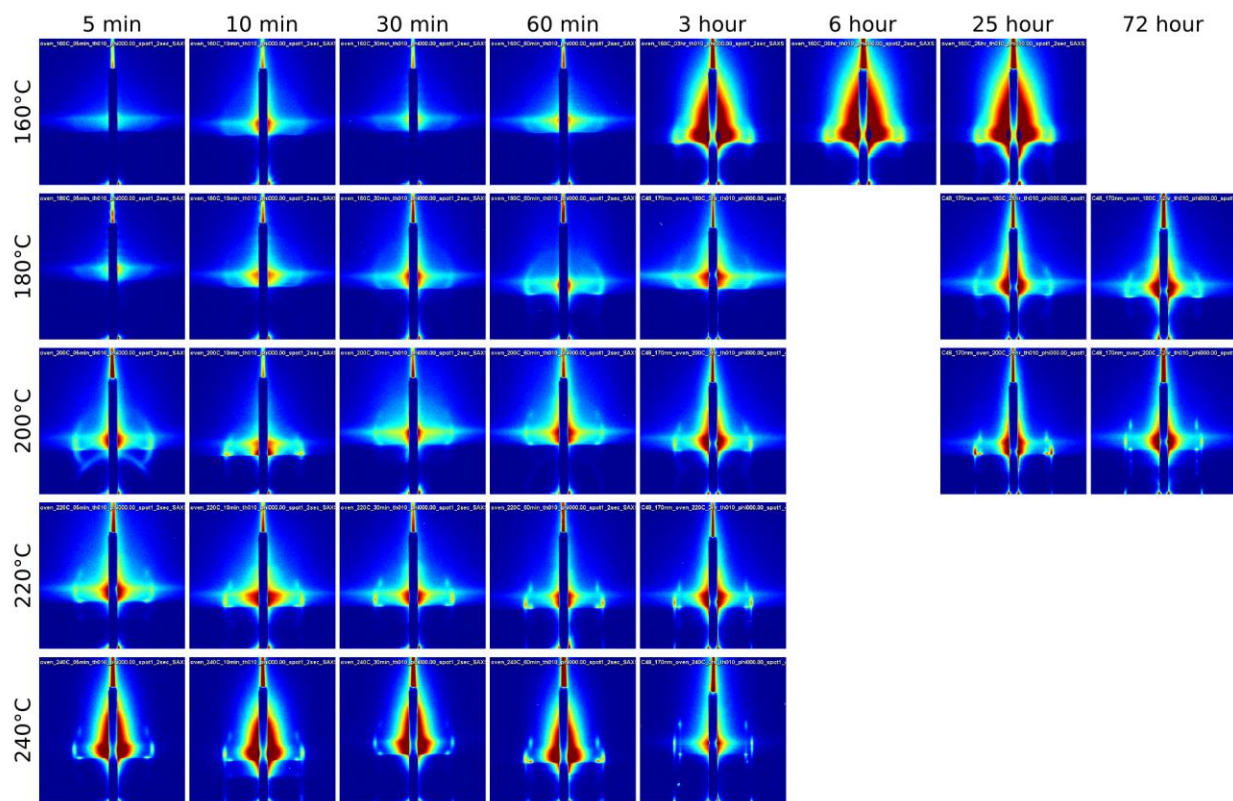


Figure S2: GISAXS of BCP thin films, measured at $\vartheta = 0.10^\circ$. These measurements are near the film-vacuum critical angle.

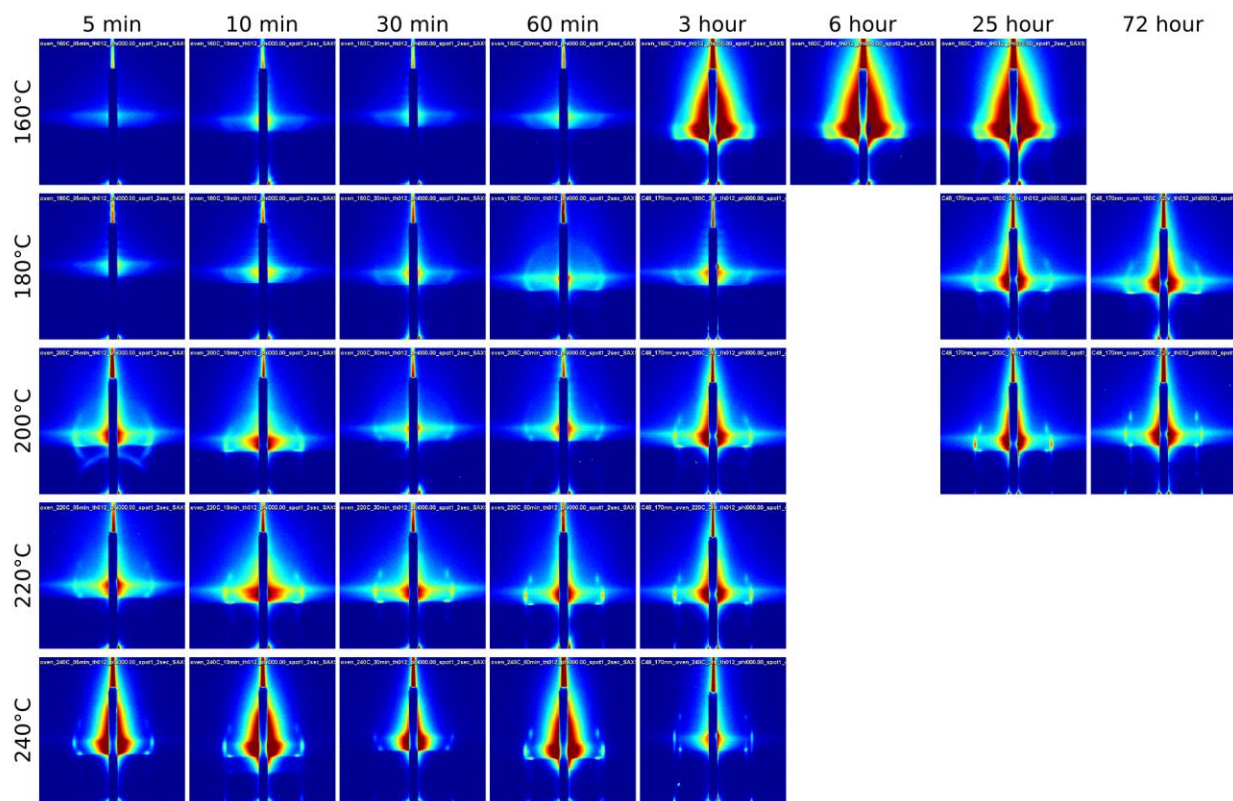


Figure S3: GISAXS of BCP thin films, measured at $\vartheta = 0.12^\circ$. These measurements are near the film-vacuum critical angle.

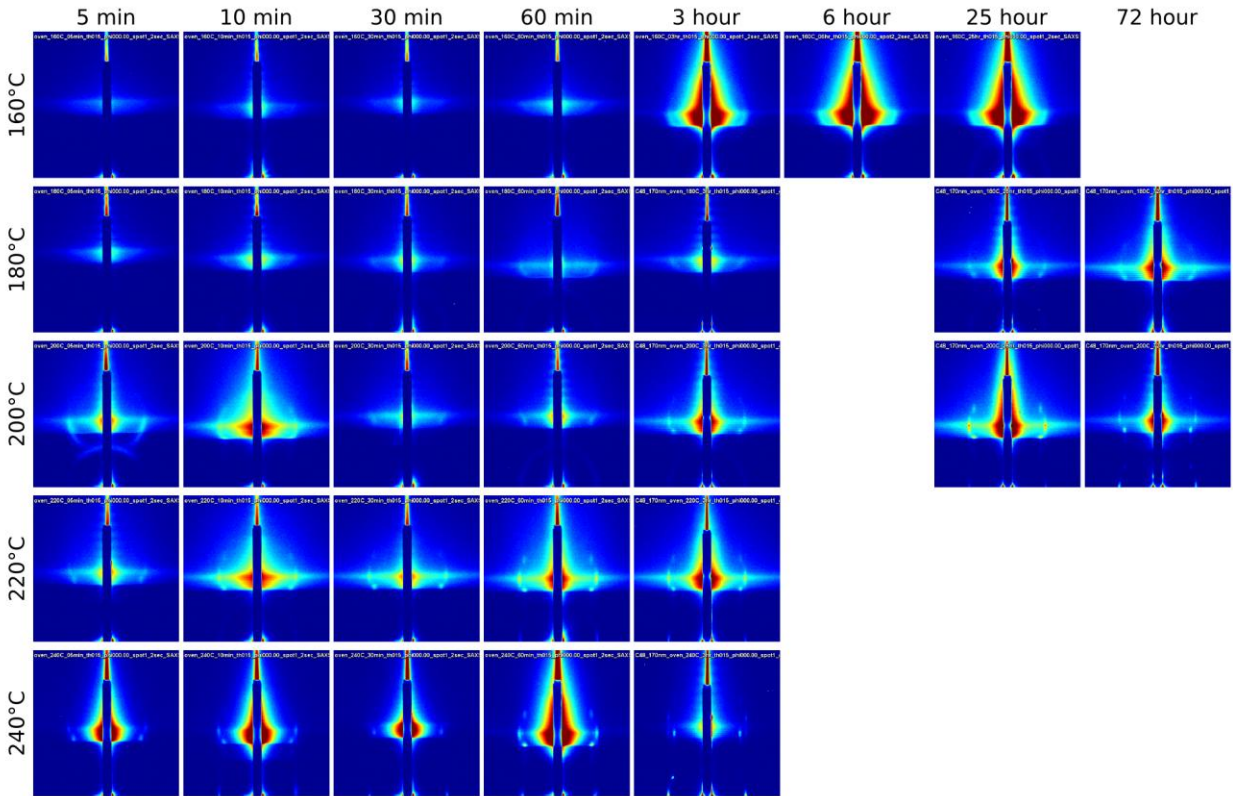


Figure S4: GISAXS of BCP thin films, measured at $\vartheta = 0.15^\circ$. These measurements are above the film-vacuum critical angle, and thus representative of the entire film thickness. The scattering patterns are consistent with data obtained below the critical angle (surface sensitive), which suggests the structures observed at the surface are consistent with the sub-surface ordering.

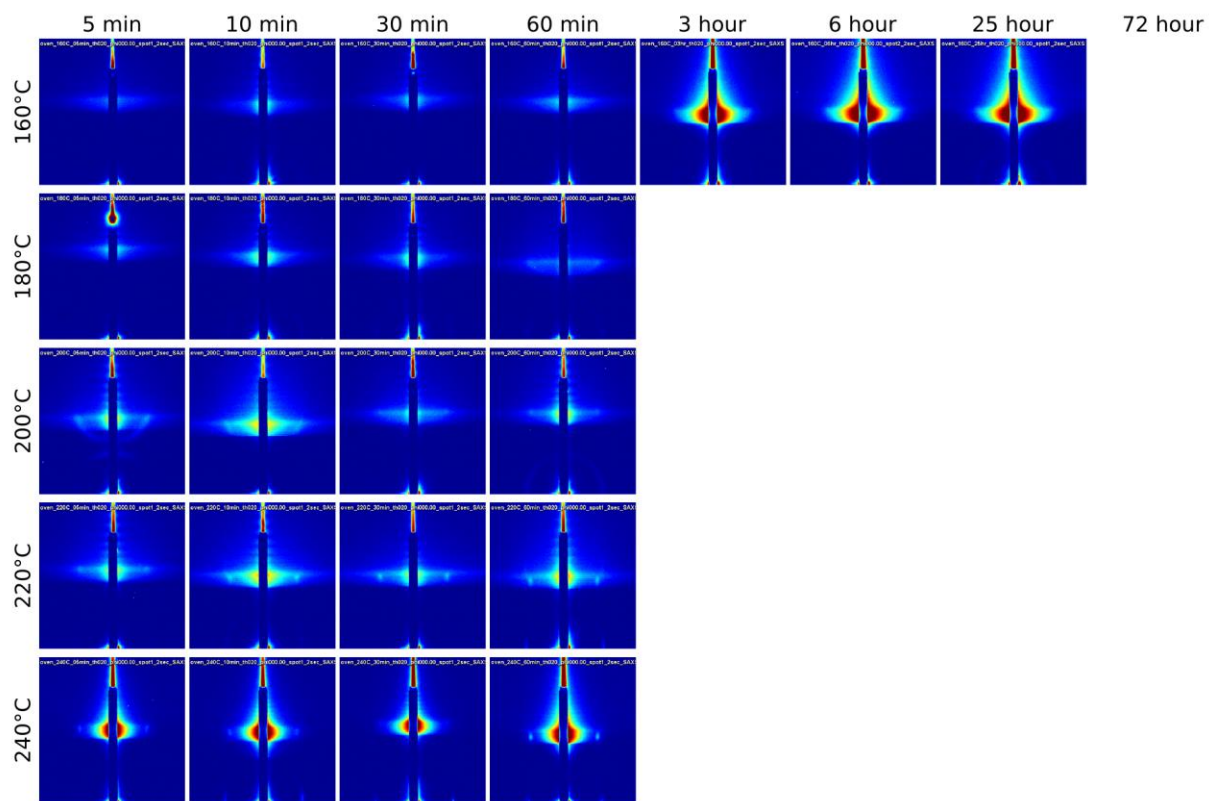


Figure S5: GISAXS of BCP thin films, measured at $\theta = 0.20^\circ$. These measurements are well above the film-vacuum critical angle. The overall intensity is decreased because of the higher angle.

SEM Analysis of Oven Annealed Thin Films

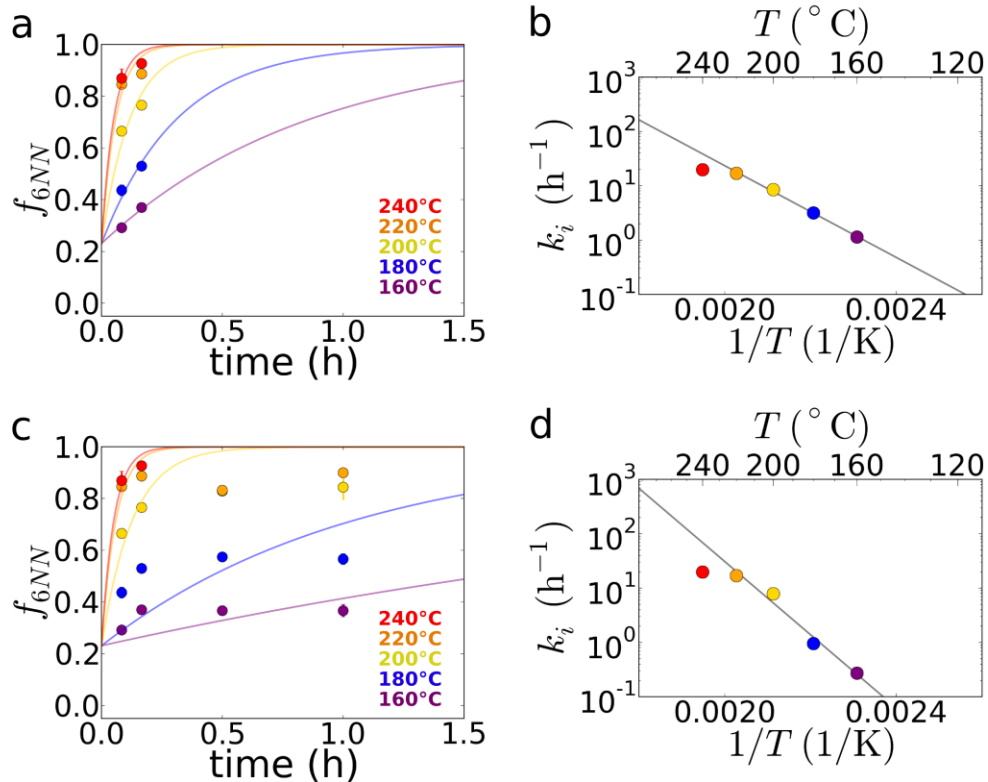


Figure S6: Kinetics of reordering from randomly-packed cylinders to hexagonally-packed cylinders. The fraction of BCP cylinders that have 6 nearest-neighbors (and are thus hexagonally-packed) increases with time. (a) The early-time data is fit to an exponential rise. (b) The temperature-dependence of the rates (k_i) suggests an Arrhenius-like behavior with activation energy $E_a = 81 \pm 12 \text{ kJ mol}^{-1}$ (95% confidence limit based on standard error of slope). (c) Fitting the entire time-series implies a slightly different temperature-dependence, (d), with an associated activation energy $E_a = 129 \pm 61 \text{ kJ mol}^{-1}$.

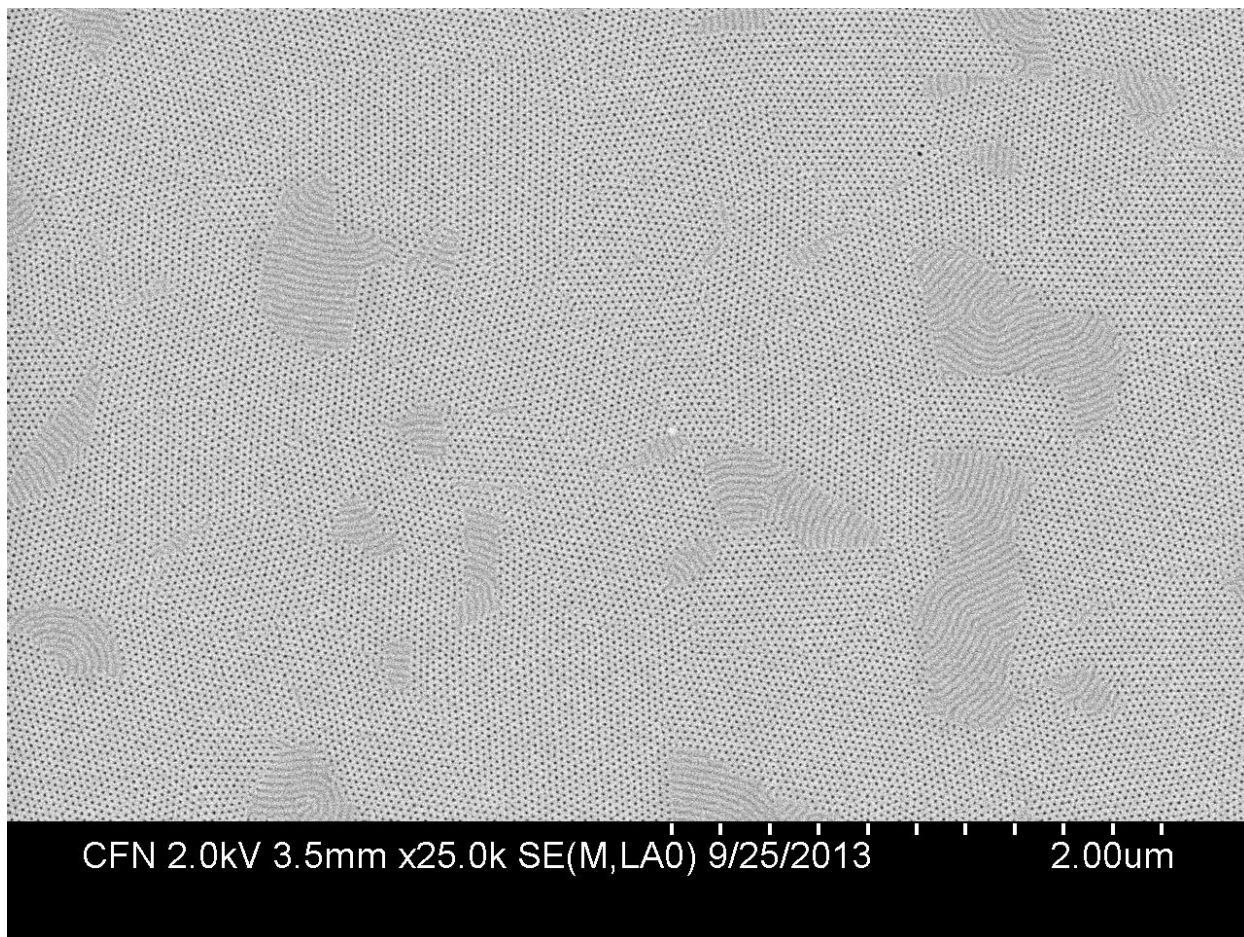


Figure S7: Conversion of vertical cylinder domains into horizontal cylinder domains during oven annealing (10 min. at 240 °C). The horizontal domains have anisotropy resulting from the preferred growth direction. As growing horizontal domains impinge on one another, they form grain boundaries.

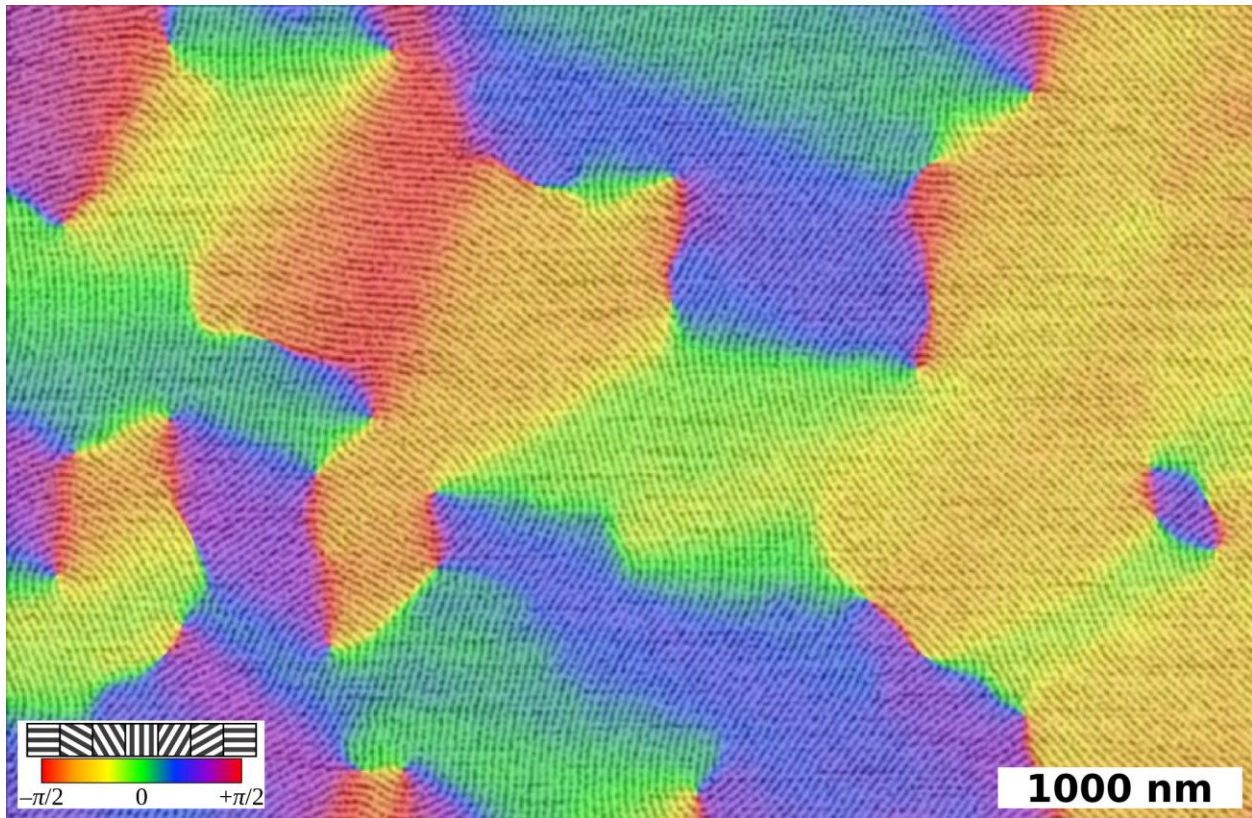


Figure S8: Example of horizontal cylinder domain obtained from oven annealing (25 h at 240 °C). The faceted (wedge/fan-like) shapes and overall grain anisotropy result from the original growth of the grains within vertical-cylinder domains.

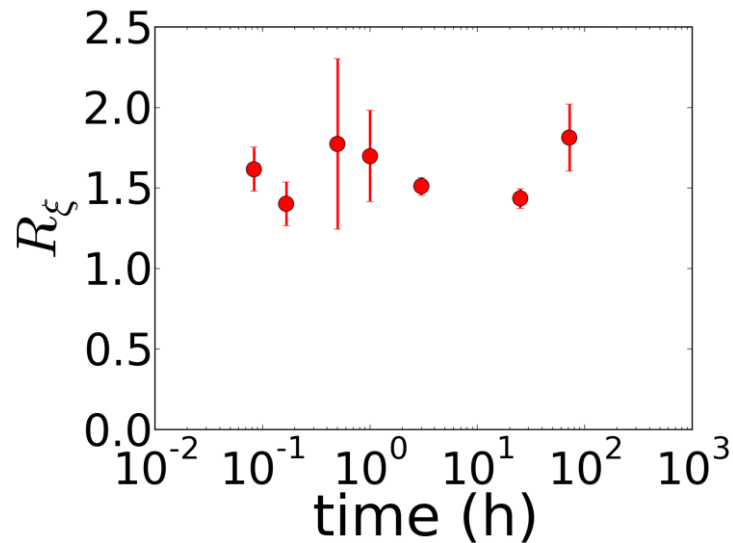


Figure S9: Grain anisotropy as a function of time, for horizontal cylinder domains during oven annealing (240 °C). The grains are anisotropic ($R_{\xi} \neq 1$), and are larger along the perpendicular direction ($R_{\xi} > 1$). The anisotropy appears roughly constant over the course of the annealing (for $t < 25$ h, the film exhibits a mixed morphology; thereafter it is predominantly or entirely composed of horizontal domains). The average value is $R_{\xi} = 1.6 \pm 0.2$.

Monte Carlo Model

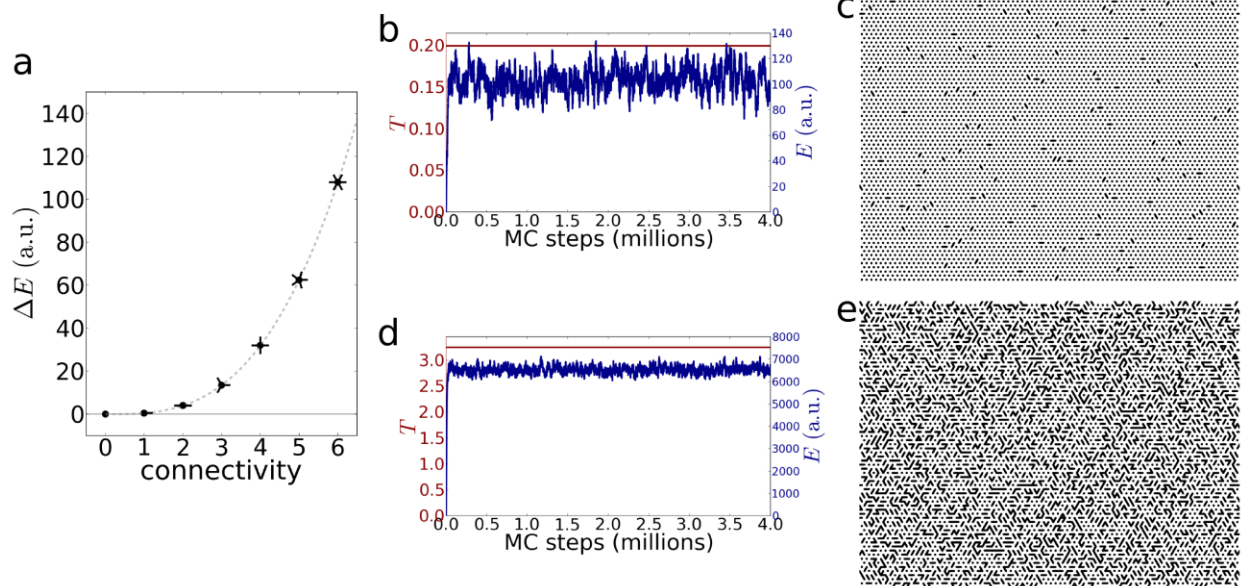


Figure S10: Monte Carlo simulation accounting for energy-penalty of defective states. (a) The relative energy of various local configurations of the lattice determines the ultimate behavior. Here, we account for the anticipated energy-penalty associated with defective states. The initial vertical cylinder state is given an energy of zero by definition (which corresponds to unconnected dots in the lattice, *i.e.* connectivity = 0). The ends of horizontal line regions are considered to be defects, with positive energy (connectivity = 1). Multiply-connected regions (connectivity 3 to 6) are defective and thus high-energy; they are assigned increasing energies according to connectivity cubed). (b) Simulation run with a simulation temperature of $T_{MC} = 0.2$; the total energy increases and remains at a steady-state value, indicative of the equilibrium number of defects that this temperature generates. (c) Corresponding snapshot of the simulation lattice. Small horizontal cylinder defects form and disappear randomly throughout the simulation. (d, e) A higher simulation temperature ($T_{MC} = 2.75$) yields a larger concentration of defects. Not surprisingly, these simulation parameters do not generate any meaningful evolution, since there is no lower-energy state available. Thus, these results are markedly unphysical. Nevertheless, the ability to temporarily form high-energy defective configurations is crucial to the ability of a BCP phase to reorder and evolve.

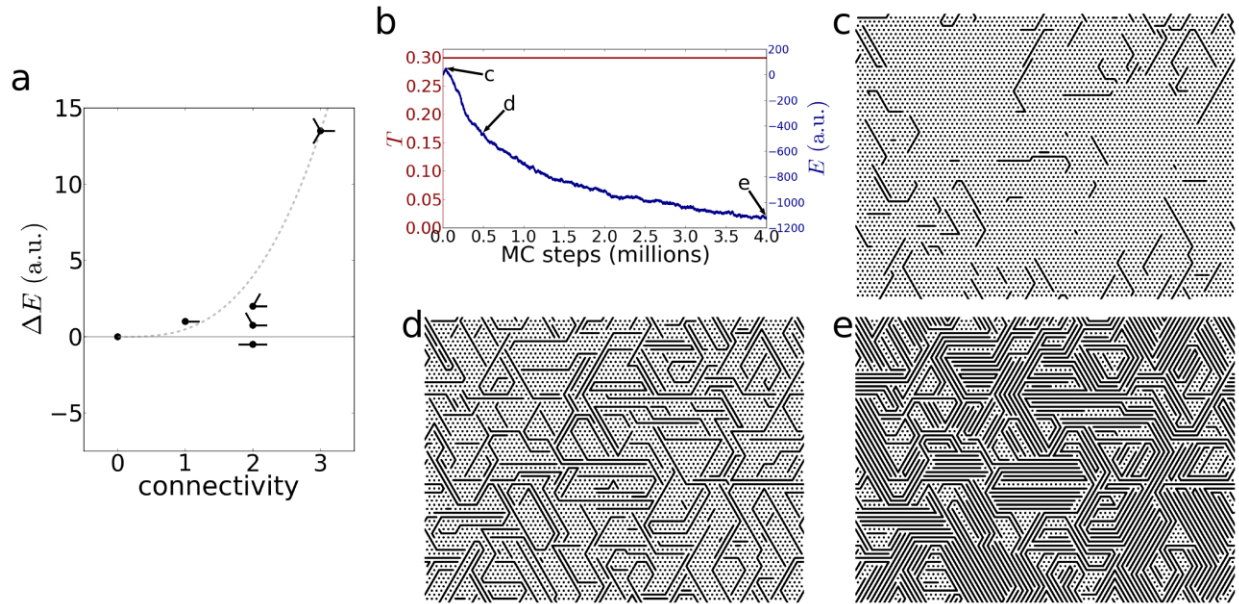


Figure S11: Monte Carlo simulation accounting for energy-gain of horizontal states. (a) The relative energy of two-connected lattice sites (which represent horizontal cylinder states) is set to be lower in energy than the initial unconnected (vertical cylinder) state. This necessarily drives the system towards the horizontal configuration. The dashed line acts as a reminder that the highly-connected local configurations are given the same higher-energy penalty as described in the previous figure. (b) During simulated annealing ($T_{MC} = 0.3$), the overall energy increases slightly (due to nucleation of high-energy defects), and then drops consistently (due to conversion of the dot-pattern into a line-pattern). Corresponding snapshots through the simulation history (c-e) are shown; their location in the annealing sequence is noted in (b). The system evolves towards a completely horizontal state, consistent with experiment. However, the details of the evolution are not consistent with experiment. In this simulation, the horizontal phase appears as individual lines, which eventually merge and stack.

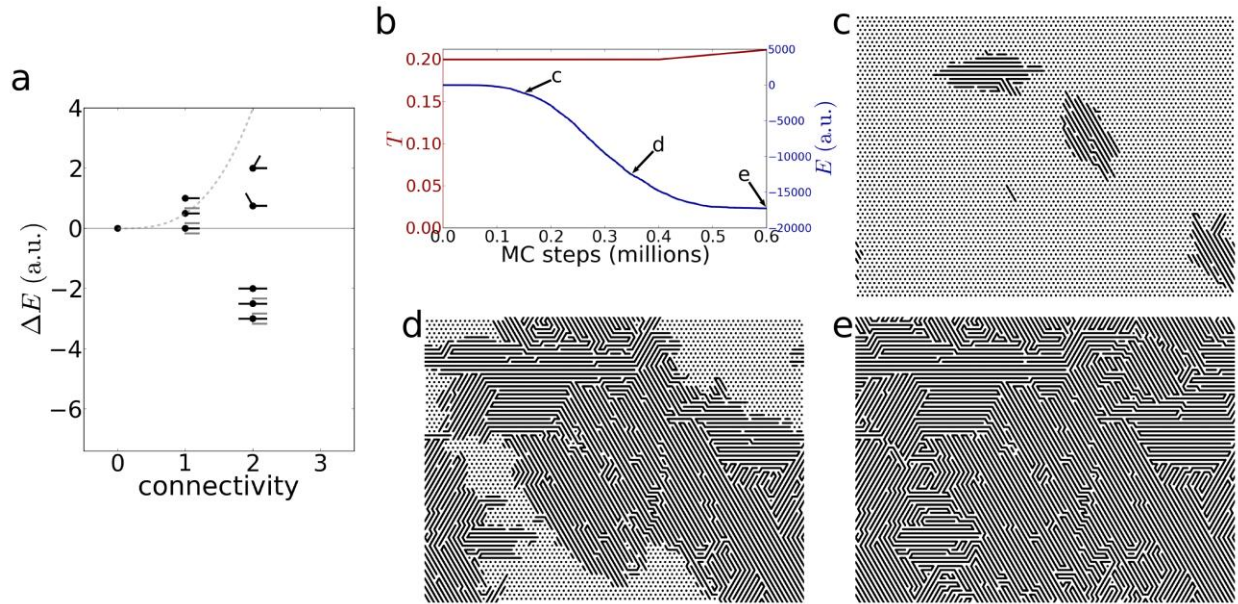


Figure S12: Monte Carlo simulation accounting for energy-gain of line stacking. (a) In this simulation, similar parameters as the previously-described simulations are used. However, an additional factor is considered: there is an energy gain (more negative) associated with having two line-patterns beside one another (the grey lines denote nearby lines, differentiating between local lines that have 0, 1, or 2 neighboring lines). (b) The annealing history ($T_{MC} = 0.2$) shows a clear lowering of energy as the system (c-e) converts to a horizontal state. In this simulation, the grains appear more physically-reasonable, exhibiting distinct boundaries. The boundaries are higher-energy than the interior (as they include connectivity = 1 defects); thus there is a natural tendency to reduce this perimeter. The grains grow somewhat anisotropically; the longer length of the initial grains along the parallel direction persists into the final fully-horizontal state (where grains are again somewhat longer along the parallel direction). Although the grain evolution is roughly similar to that observed experimentally, the grain anisotropy does not match experiments for PS-*b*-PMMA.

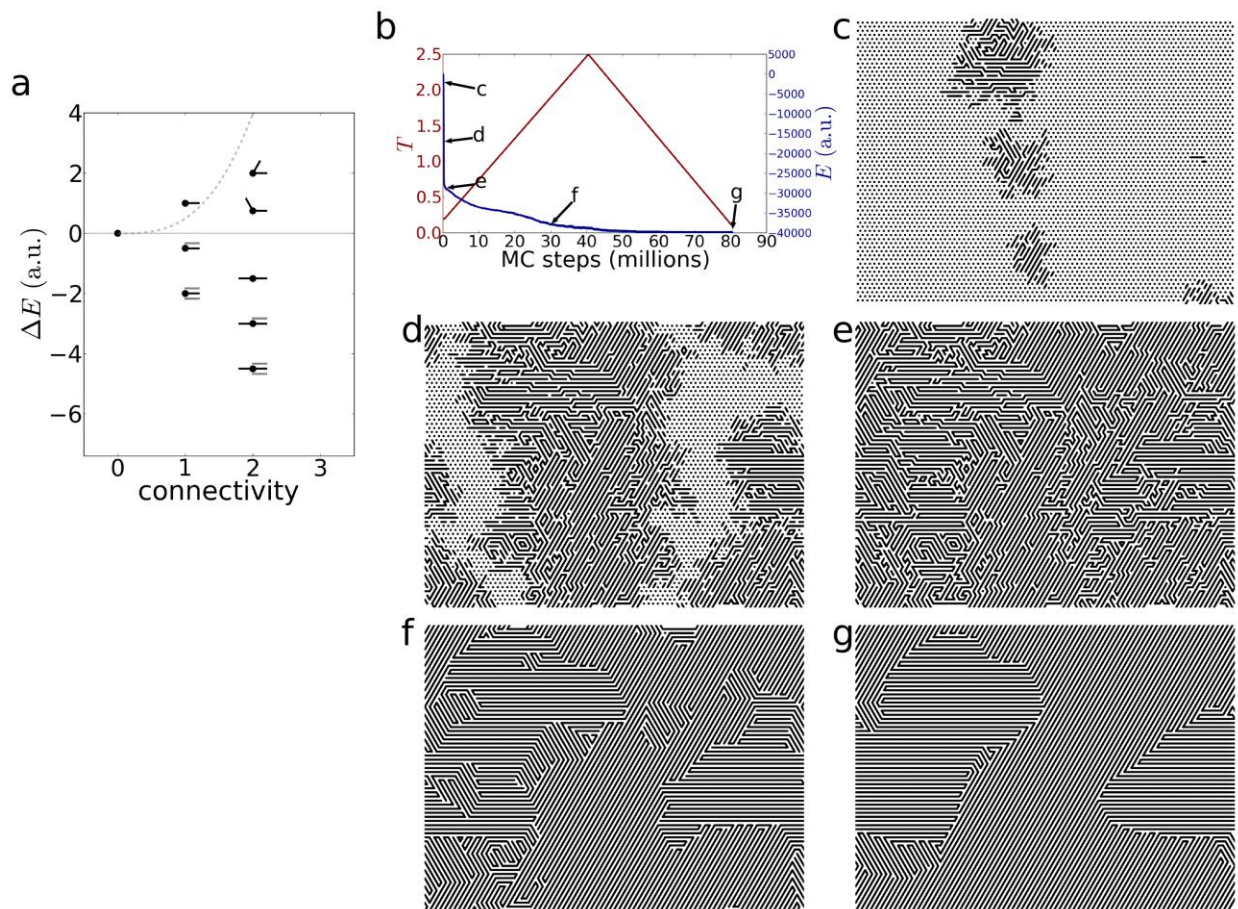


Figure S13: Monte Carlo simulation. (a) In this simulation, the (negative) energy gain for nearby parallel configurations is larger. (b) The annealing history shows a clear lowering of energy as the system (c-g) converts to a horizontal state. In this simulation, the stronger energetic preference for nearby parallel lines leads to grains that are more isotropic. That is, there is a roughly equal propensity for grains to grow in the parallel and perpendicular directions.

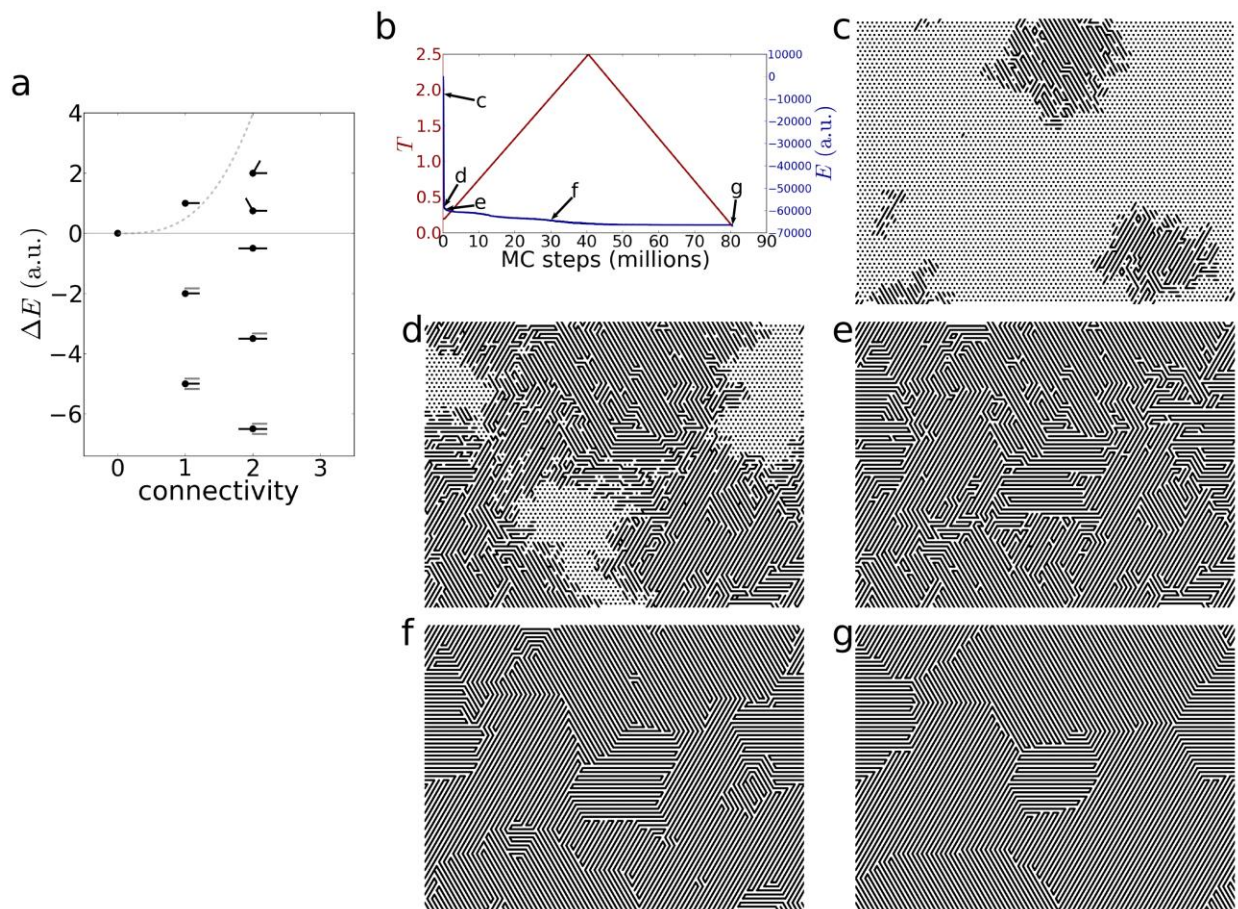


Figure S14: Monte Carlo simulation. (a) In this simulation, the (negative) energy gain for nearby parallel configurations is larger than in all previous examples. (b) The annealing history shows a clear lowering of energy as the system (c-g) converts to a horizontal state. In this simulation, the very strong energetic preference for nearby parallel lines leads to grains that are longer along the *perpendicular* direction. There is a strong driving force to generate locally stacked-line configurations, which yields early-stage grains that are anisotropic, and late-stage horizontal domains that are similarly longer along the perpendicular direction (orthogonal to the cylinder/line long axis). This matches the experimentally-observed grain anisotropy for PS-*b*-PMMA.

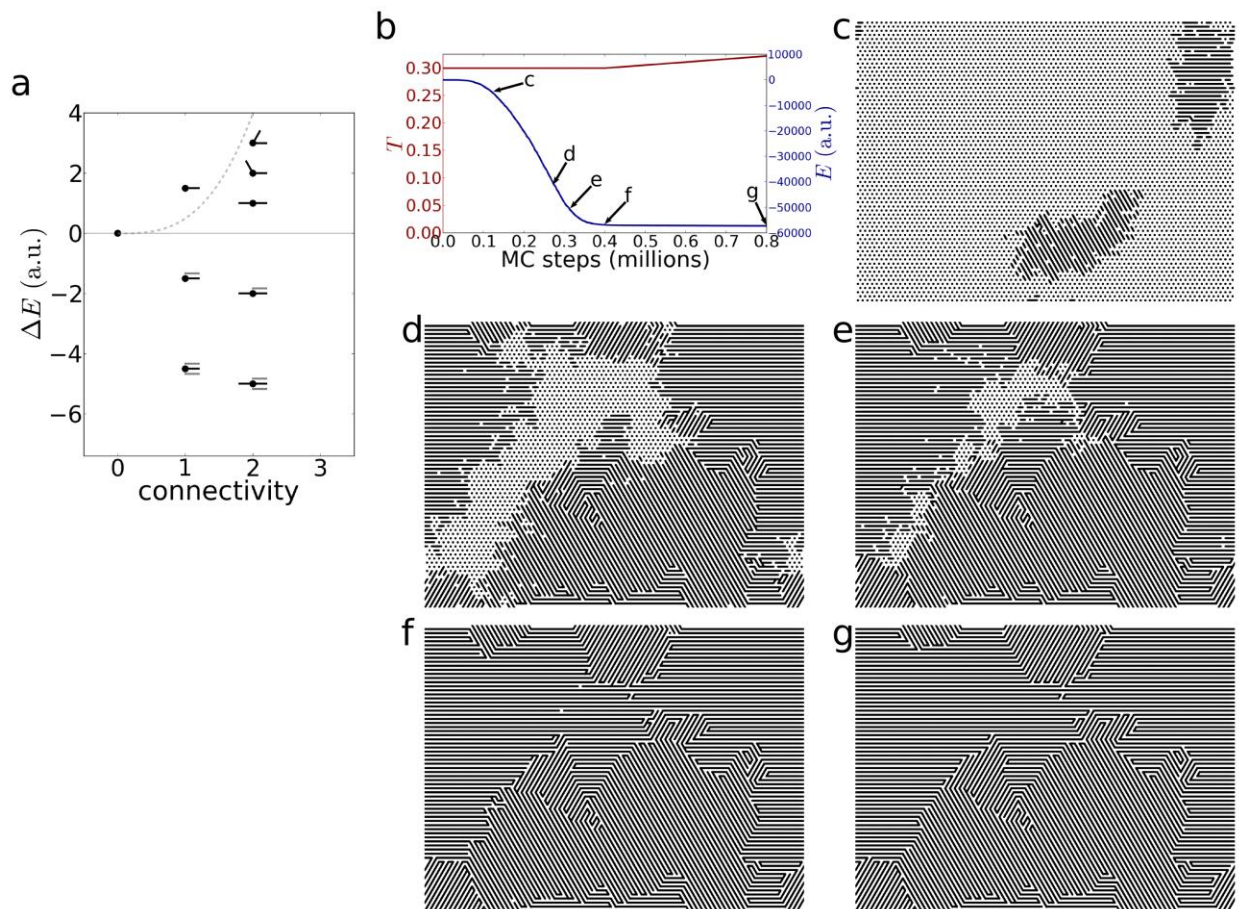


Figure S15: Monte Carlo simulation. (a) In this simulation, the (negative) energy gain for nearby parallel configurations is large (as before). Additionally, the energy for lines without neighboring lines (*i.e.* connectivity = 2 regions without nearby parallel lines) is set to be *positive*. This makes isolated lines act as high-energy defects, which can arise intermittently but are disfavored at equilibrium. (b) The annealing history shows a clear lowering of energy as the system (c-g) converts to a horizontal state. In this simulation, the energetic balance leads to strongly anisotropic grains (longer along perpendicular direction), with overall shapes and anisotropy consistent with experimental results on PS-*b*-PMMA. For instance, the simulation correctly captures the ‘fan’ shapes of grains in the final fully-horizontal state.

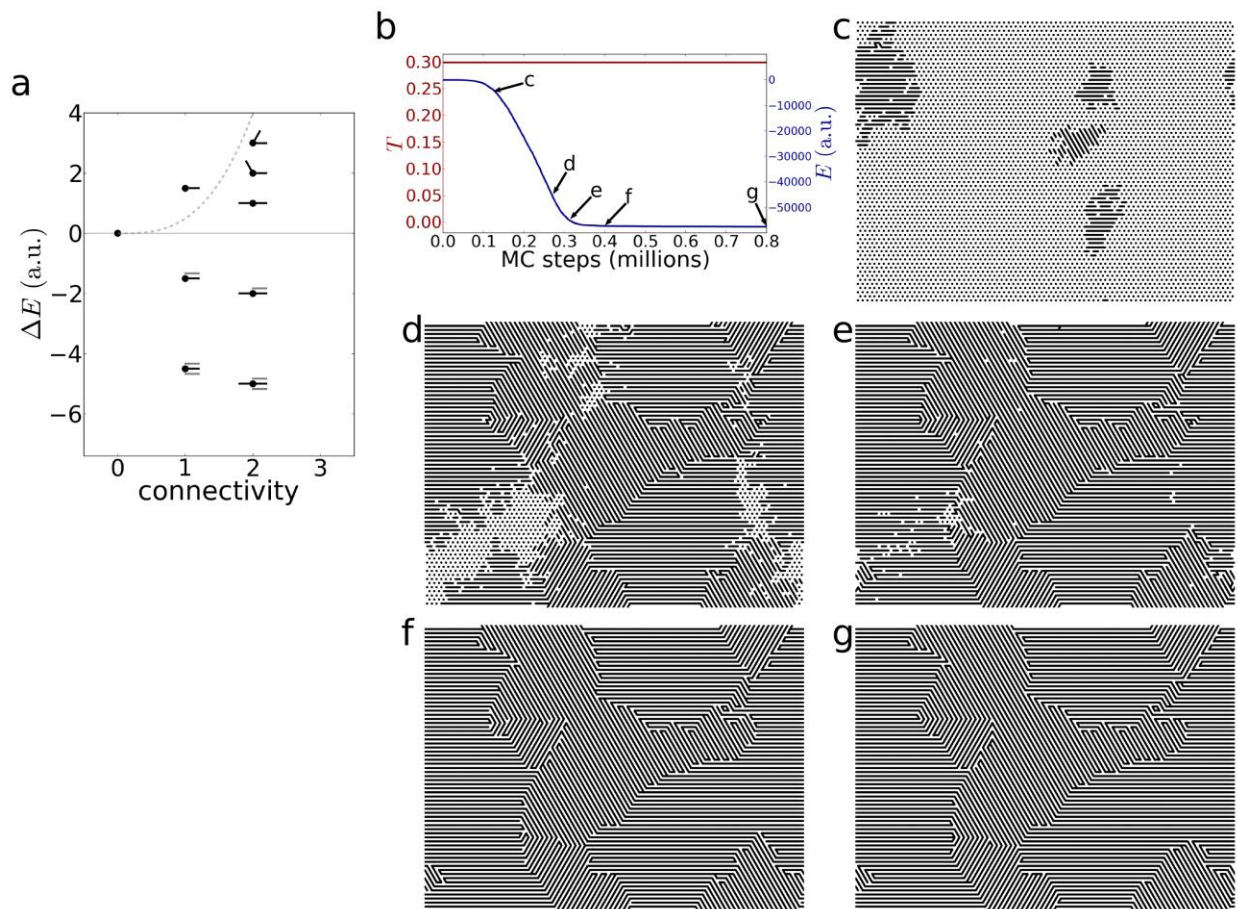


Figure S16: Monte Carlo simulation. This is a replicate of the simulation shown in the previous figure. (a) The (negative) energy gain for nearby parallel configurations is large, and lines without neighboring lines have a positive energy contribution. (b) The annealing history shows a clear lowering of energy as the system (c-g) converts to a horizontal state. In this simulation, the energetic balance leads to strongly anisotropic grains (longer along perpendicular direction), with overall shapes and anisotropy consistent with experimental results on PS-*b*-PMMA.

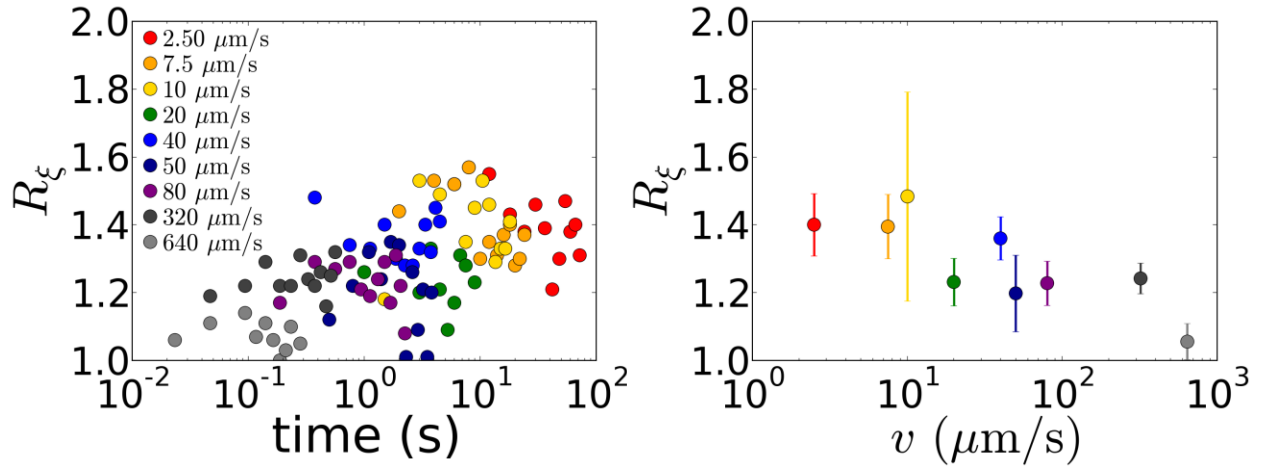


Figure S17: Grain anisotropy for LZA frozen zone samples. (left) Grain anisotropy during an LZA heating experiment. The legend indicates the various laser sweep velocities; the time is computed from the moment when the film crosses through the glass-transition temperature (T_g). Within any given LZA ordering history, the grain anisotropy is roughly constant (consistent with oven annealing results). However, the grain anisotropy varies with sweep velocity (*i.e.* heating rate). (right) The corresponding average grain anisotropies for the various LZA sweep rates.

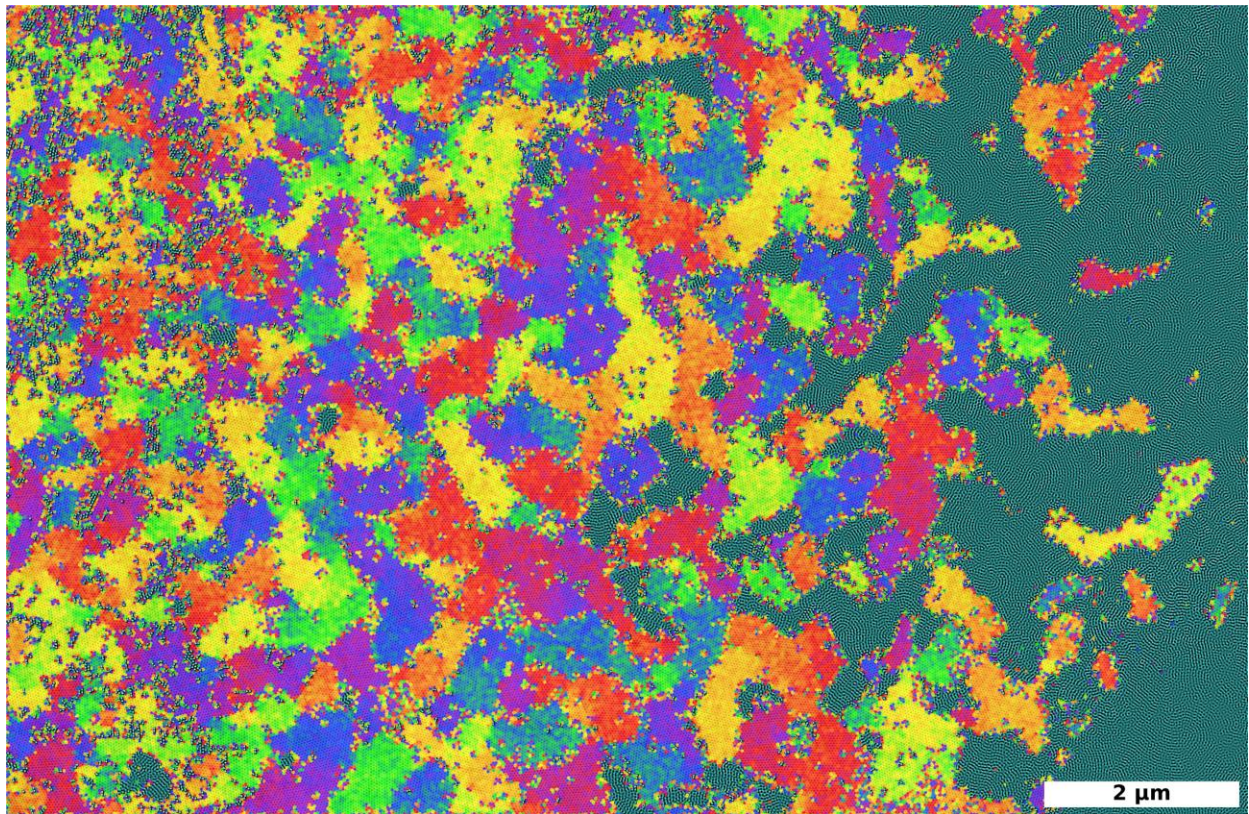


Figure S18: SEM of BCP ordering during LZA. Representative image from a ‘frozen zone’ LZA sample, with sweep velocity $v = 1.25 \mu\text{m/s}$. The vertical cylinder domains are color-coded based on grain orientation. The horizontal domains are Fourier filtered and highlighted in blue. The selected image is from the region where vertical cylinders are converting to horizontal ($30 \mu\text{m}$ in advance of the center of the laser line). The center of the image had reached a local temperature of $284 \text{ }^\circ\text{C}$ when annealing was terminated (annealing had proceeded for 413 s, since the sample was heated above T_g).

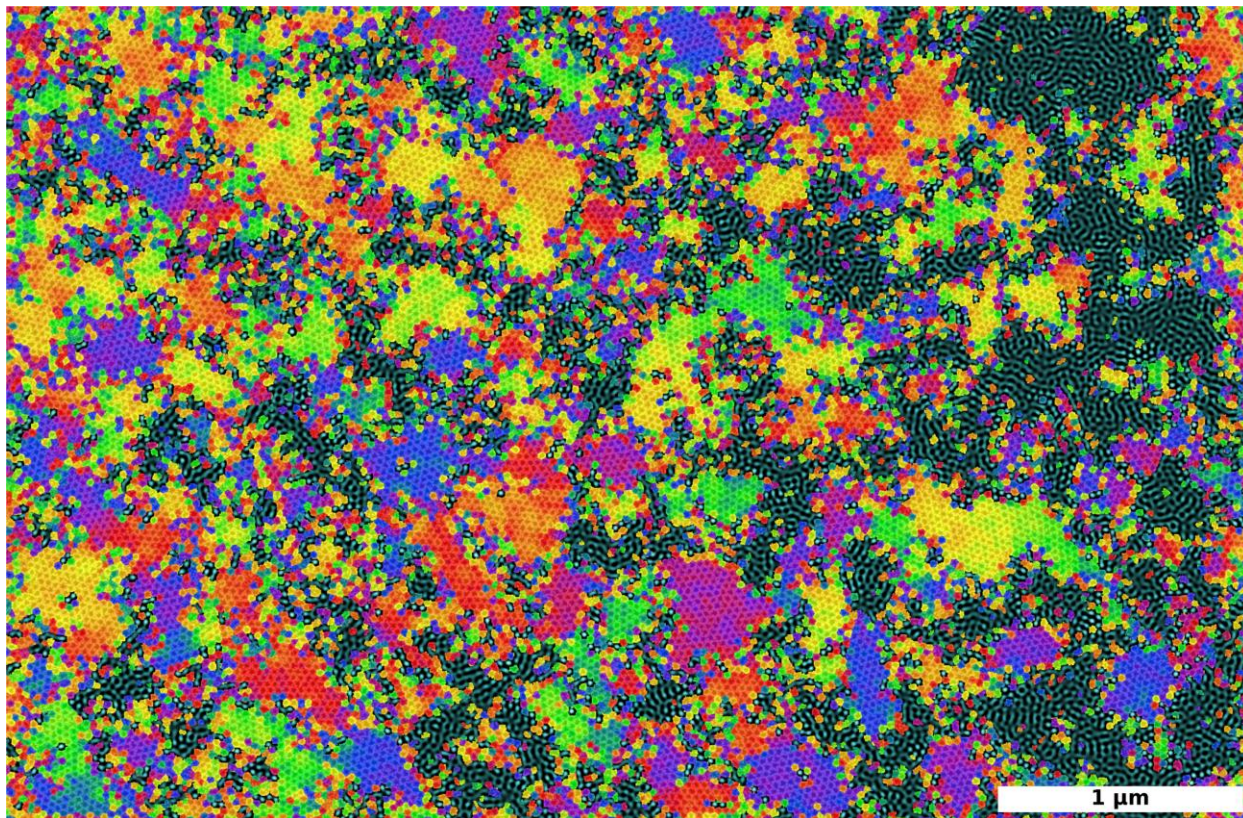


Figure S19: SEM of BCP ordering during LZA. Representative image from a ‘frozen zone’ LZA sample, with sweep velocity $v = 10 \mu\text{m/s}$. The vertical cylinder domains are color-coded based on grain orientation. The horizontal domains are Fourier filtered and highlighted in blue. The selected image is from the region where vertical cylinders are converting to horizontal ($30 \mu\text{m}$ in advance of the center of the laser line). The center of the image had reached a local temperature of $284 \text{ }^\circ\text{C}$ when annealing was terminated (annealing had proceeded for 52 s, since the sample was heated above T_g).